

Article

Using Amorphous CoB Alloy as Transducer to Detect Acoustic Propagation and Heat Transport at Interface

Liu Jian ¹ and Gyung-Min Choi ^{1,2,*} ¹ Department of Energy Science, Sungkyunkwan University, Suwon 16419, Korea; cfluijian@outlook.com² Center for Integrated Nanostructure Physics, Institute for Basic Science (IBS), Suwon 16419, Korea

* Correspondence: gmchoi@skku.edu; Tel.: +82-31-299-6279

Featured Application: The use of an amorphous CoB alloy for the transducer layer to measure the acoustic and thermal properties of the soft layer.

Abstract: Acoustic oscillation provides useful information regarding the interfacial coupling between metal transducer layers and substrate materials. The interfacial coupling can be significantly reduced by a mechanically soft layer between the transducer and substrate. However, preserving a thin, soft layer at the interface during fabrication is often challenging. In this study, we demonstrate that an amorphous CoB alloy on top of a sapphire substrate can substantially amplify acoustic oscillations. By analyzing the attenuation of acoustic oscillations, we show that a thin, soft layer with a thickness of $>2 \pm 1 \text{ \AA}$ exists at the interface. The intermediate layer at the interface is further verified by investigating heat transport. By analyzing the slow decrease of the temperature of the transducer layer, we determine a thermal conductance of $35 \pm 5 \text{ MW m}^{-2} \text{ K}^{-1}$ at the transducer/substrate interface. This low value supports the existence of a thin, soft layer at the interface. Our results demonstrate that an amorphous metal with B alloying effectively preserves the soft nature at the interface and detects the acoustic propagation and heat transport across it.



Citation: Jian, L.; Choi, G.-M. Using Amorphous CoB Alloy as Transducer to Detect Acoustic Propagation and Heat Transport at Interface. *Appl. Sci.* **2021**, *11*, 5155. <https://doi.org/10.3390/app11115155>

Academic Editor: Filippo Berto

Received: 27 April 2021

Accepted: 31 May 2021

Published: 1 June 2021

Publisher's Note: MDPI stays neutral with regard to jurisdictional claims in published maps and institutional affiliations.



Copyright: © 2021 by the authors. Licensee MDPI, Basel, Switzerland. This article is an open access article distributed under the terms and conditions of the Creative Commons Attribution (CC BY) license (<https://creativecommons.org/licenses/by/4.0/>).

Keywords: acoustic wave; picosecond acoustics; interfacial layer; thermal conductance

1. Introduction

An acoustic wave is the propagation of strain in a condensed matter, and its propagation speed is determined by the group velocity of low-energy phonons; that is, the speed of sound. Time-resolved measurements of acoustic waves based on short-pulsed lasers, a time-resolved measurement of acoustic waves, often called “picosecond acoustics” or “picosecond ultrasonics”, have been employed to investigate thickness information [1–5], elastic properties [6–10], phonon properties [11–15], and interfacial quality [16–19]. For example, a time delay between acoustic echoes can be used to accurately determine the thickness of a metal layer on top of an insulating substrate [1–5]. In addition, the interfacial quality between two layers has been investigated from the perspectives of the amplitude and attenuation of acoustic waves [16–19]. To obtain a strong acoustic signal, a large acoustic mismatch is required. However, many condensed solid phases have a similar acoustic impedance, and acoustic oscillations are often suppressed. Inserting a mechanically soft layer with a small acoustic impedance between two layers can enhance acoustic oscillations, but a soft layer with a thickness of a few nanometers is prone to fabrication damage.

A thin, soft layer at the interface affects not only acoustic propagation but also heat transport. A relatively well-studied system is the strongly coupled interface between two hard materials, such as metals and oxides; thermal conductances at interfaces have been explained by phonon scattering at interfaces and the phonon spectrum of constituent materials [20–23]. A weakly coupled interface has been achieved by inserting a thin polymer or two-dimensional material at the interface [19,24]. It has been reported that the thermal conductance of the weakly coupled interface strongly depends on the stiffness of

interfacial bonds [24,25]. However, the intrinsic nature of interfacial bonds may depend on the preparation method for the insertion layer [26] and the deposition process for the transducer layer.

In this work, we use the $\text{Co}_{50}\text{B}_{50}$ (atomic %) alloy as a transducer to detect the propagation of acoustic waves and thermal energy across an interface. Boron (B) is a glass-forming element, and alloying it with a ferromagnetic metal, such as Co, Fe, and Ni, results in an amorphous structure. The amorphous ferromagnet shows improved magnetic properties, such as higher magnetic susceptibility, smaller coercivity, and a smaller eddy current [27]. In addition, amorphous metals can have improved mechanical properties, such as high tensile yield strengths, high elastic strain limits, and a smooth interface with an underlying oxide [28,29]. In this work, we demonstrate that the $\text{Co}_{50}\text{B}_{50}$ transducer can drastically enhance acoustic waves compared to the single element of Co. The strong acoustic oscillation results from a soft intermediate layer between $\text{Co}_{50}\text{B}_{50}$ and the substrate. By analyzing the frequency and damping of acoustic oscillations using acoustic modeling, we determine the thickness of the intermediate layer to be $>2 \pm 1 \text{ \AA}$. We expect that the soft intermediate layer is preserved by low kinetic damage during the $\text{Co}_{50}\text{B}_{50}$ deposition.

We also investigate the heat transport at the interface by measuring the temperature response of the $\text{Co}_{50}\text{B}_{50}$ transducer. Owing to its magnetic property, we were able to collect the temperature response of the transducer without contamination by any signal from the substrate. By analyzing the temperature response using thermal modeling, we determine the interfacial thermal conductance of $35 \pm 5 \text{ MW m}^{-2} \text{ K}^{-1}$, which is one order of magnitude smaller than that of the strongly coupled interface. This low thermal conductance supports the existence of the thin, soft layer at the interface. Our results show that the amorphous $\text{Co}_{50}\text{B}_{50}$ alloy is an ideal choice for a transducer layer to investigate acoustic propagation and heat transport across a thin, soft layer.

2. Materials and Methods

We fabricated the sap/Co (10 nm)/Pt (2 nm) and sap/ $\text{Co}_{50}\text{B}_{50}$ /(5~15 nm)/Pt (4 nm) structure using a magnetron sputter with a base pressure of $<2 \times 10^{-7}$ Torr. The sap layer was a sapphire substrate with an orientation of (0001). The Co or $\text{Co}_{50}\text{B}_{50}$ layer acted as a transducer for acoustic waves. The Pt layer acted as a layer that protected Co or $\text{Co}_{50}\text{B}_{50}$ from oxidation. All metal layers were deposited with an Ar pressure of 3 mTorr, a target-to-substrate distance of 100 mm, and a typical deposition rate of 0.02 nm s^{-1} . The deposition rate of each layer was predetermined with a single, thick layer, whose thickness was determined by X-ray reflectivity measurements; then, the thickness of each layer was controlled by deposition time. We used a pure element target for the deposition of the Co and Pt layers and a CoB alloy target with an equiatomic composition for deposition of the $\text{Co}_{50}\text{B}_{50}$ layer. All layers were deposited at room temperature. The lateral sizes of all samples were around 10 mm.

We did not use a special treatment, such as chemical cleaning or pre-annealing, for the substrate. Therefore, a thin, soft layer, such as a polymer, naturally formed on top of the substrate. However, such a thin, soft layer is usually destroyed during the sputtering process because of the high kinetic energy of the sputtered elements, and thus a strong coupling between the deposited layer and substrate is usually achieved. The kinetic energy of the sputtered elements depends critically on the surface binding energy, as follows:

$$f(E) \propto \frac{E}{(E + E_{\text{sb}})^3}, \quad (1)$$

where $f(E)$ is the number fraction of sputtered elements, E is the kinetic energy of the sputtered elements, and E_{sb} is the surface binding energy of the target material with a typical magnitude of a few electronvolts [30]. The schematics for the sputtering process and energy distribution of sputtered elements are shown in Figure 1.

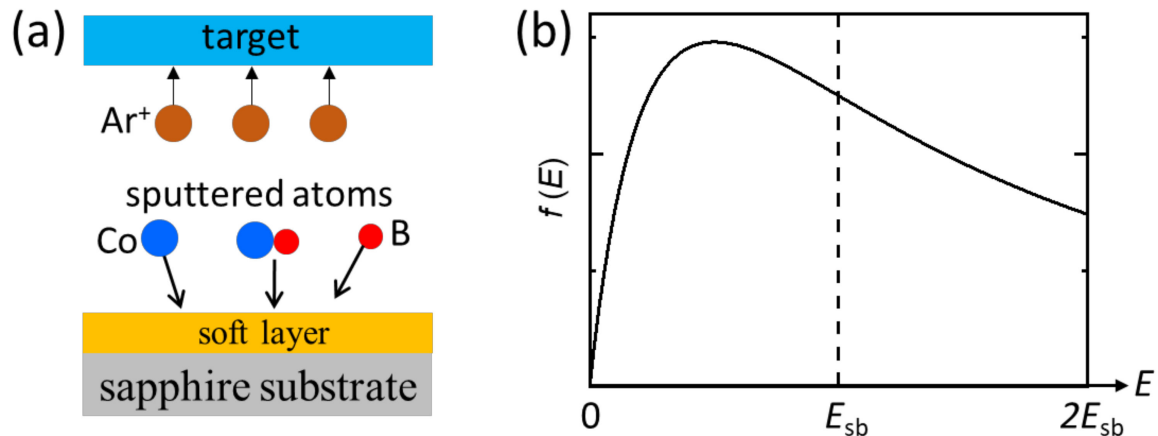


Figure 1. (a) Schematics for the sputtering process. An Ar^+ ion bombards the CoB alloy target. Target elements are ejected from the target surface and deposited on the substrate. (b) The number distribution (f) of the sputtered elements from the target surface is a function of the kinetic energy (E). The maximum f occurs at E with around half the surface binding energy (E_{sb}) of the target material.

To investigate the propagation of acoustic waves at the interface, we measured the change of reflectivity (ΔR) from the transducer layer as a function of time [1–19]. When a pump pulse thermally excites the metal transducer, a strain pulse is introduced in the transducer. A probe pulse has a time delay from the pump pulse, measured as ΔR , caused by the changes of temperature (ΔT) and strain ($\Delta \epsilon$) of the transducer layer. ΔR arising from $\Delta \epsilon$ is easily distinguished from that arising from ΔT because $\Delta \epsilon$ oscillates rapidly, whereas ΔT changes slowly. ΔR arising from ΔT can be employed to investigate the heat transport from the transducer layer to substrate [31]. However, when the transducer is thinner than the penetration depth of the probe light, ΔT corresponding to both the transducer layer and substrate affects ΔR ; thus, the thermal analysis becomes extremely complicated.

To investigate the heat transport at the interface, we measured the magneto-optic Kerr effect (MOKE) from the transducer layer as a function of time [32,33]. When the transducer layer is a ferromagnet, the polarization of the reflected probe light rotates, and the rotation angle ($\Delta \theta$) is proportional to the change in magnetization (ΔM). When ΔM is caused by heating and the resulting ΔT is small enough, a linear relationship between $\Delta \theta$ and ΔT is achieved [32,33]. Because the sapphire substrate was not a ferromagnet, only the transducer layer contributed to $\Delta \theta$ regardless of the transducer thickness.

For the pump and probe pulses, we used a Ti:sapphire laser oscillator that produced 0.1 ps laser pulses with a repetition rate of 80 MHz and a wavelength of 785 nm. The generated laser was immediately divided into pump and probe beams using a polarized beam splitter. A mechanical delay stage controlled the time delay between the pump and probe pulses. To increase the signal-to-noise ratio of detection, we modulated the pump/probe at 1 MHz/200 Hz with an electro-optic modulator (EOM)/optical chopper. Due to the group velocity dispersion of the EOM, the pulse width of the pump pulse was increased to 1.2 ps. We irradiated the pump and probe beams on the transducer surface at a spot size of $6 \mu\text{m}$ with incident fluences of 6 and 0.6 J m^{-2} , respectively, for pump and probe. After reflection from the transducer layer, ΔR and $\Delta \theta$ values of the probe were collected by a normal and balanced photodetector, respectively. The raw signal from the balanced detector showed a small contribution from ΔR . To collect the pure MOKE signal, we measured $\Delta \theta$ with magnetic fields of + and -0.5 T , and then collected the difference between them. When we changed the direction of magnetization with magnetic fields, $\Delta \theta$ changed its sign, whereas ΔR did not. The schematic of the measurement setup is shown in Figure 2.

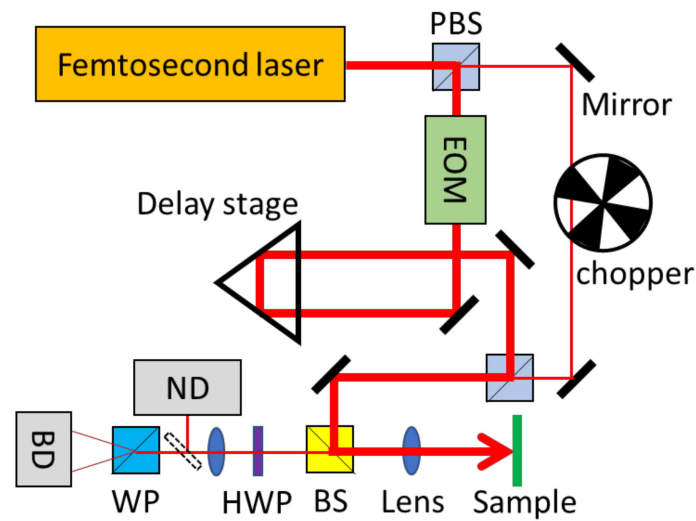


Figure 2. The pump-probe experimental set-up. A pulsed laser was split to the pump (thick red line) and probe (thin red line) via a polarizing beam splitter (PBS). The pump and probe were modulated via an electro-optic modulator (EOM) and optical chopper, respectively. The time delay between the pump and probe was controlled by a delay stage. The pump and probe were focused on the transducer surface by a lens. The reflection from the probe, after the non-polarizing beam splitter (BS), was collected by a normal detector (ND) for ΔR measurement and by a balanced detector (BD) for $\Delta\theta$ measurement. For $\Delta\theta$ measurement, a halfwave plate (HWP) and Wollaston prism (WP) were used to control the polarization of the probe beam.

3. Results

3.1. Acoustic Propagation at Interface

We compared the ΔR responses of the Co and $\text{Co}_{50}\text{B}_{50}$ transducers (Figure 3a). In the case of the Co transducer, ΔR showed a typical temperature response (ΔR arising from ΔT) without any acoustic oscillations (ΔR arising from $\Delta\epsilon$): a rapid increase in ΔT at zero time delay by the pump pulse, followed by a gradual decrease because of slow heat dissipation to the substrate (Figure 3b). In contrast, the $\text{Co}_{50}\text{B}_{50}$ transducer showed a strong acoustic oscillation in addition to the slow temperature response (Figure 3c). The magnitude of acoustic oscillation was similar to that of the temperature signal.

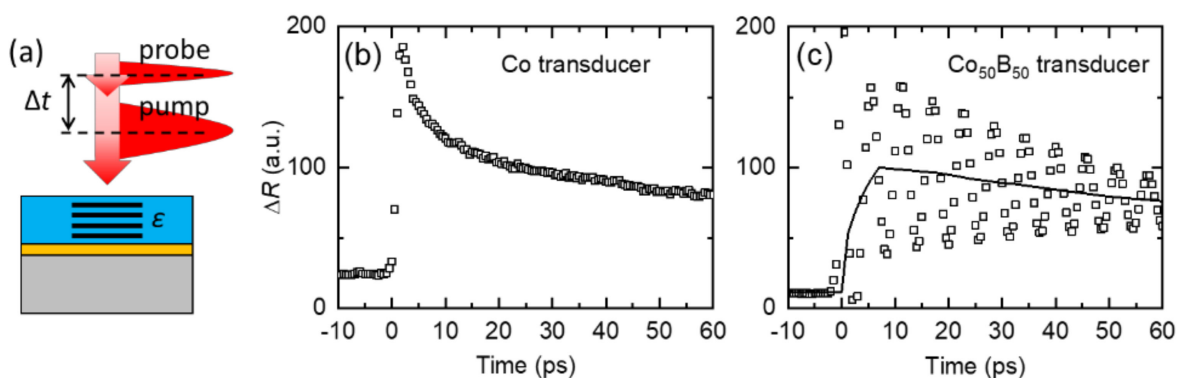


Figure 3. ΔR comparison of the Co and $\text{Co}_{50}\text{B}_{50}$ transducers. (a) Schematics for detection of ΔR , which was caused by changes in the strain (ϵ). The blue/orange/gray layers represent the transducer/interface/substrate, respectively. ΔR results of the (b) sap/Co (10 nm)/Pt (2 nm) and (c) sap/ $\text{Co}_{50}\text{B}_{50}$ (10 nm)/Pt (4 nm) sample. The black squares are experimental data. The black line in (b) represents the background temperature signal.

By subtracting the temperature signal from the raw data, we were able to extract acoustic oscillations. Then, we compared the acoustic oscillations obtained with different

Co₅₀B₅₀ thicknesses (Figure 4). The oscillations were fitted with a damped cosine function, $A \cos(2\pi ft) \exp(-t/\tau)$, where A is the oscillation amplitude, f is the oscillation frequency, t is the time delay between the pump and probe, and τ is the exponential decay time. A smaller Co₅₀B₅₀ thickness resulted in a larger f and smaller τ . Such a strong oscillation of acoustic waves indicated that acoustic waves were reflected from the sap/Co₅₀B₅₀ interface with a high reflection coefficient (r). The reflection of acoustic waves was determined by acoustic impedance, $Z = \rho v_s$, where ρ is the density of the material. When two materials with Z of Z_1 and Z_2 have infinite thicknesses, r is expressed as [34,35]

$$r = \frac{Z_1 - Z_2}{Z_1 + Z_2}. \quad (2)$$

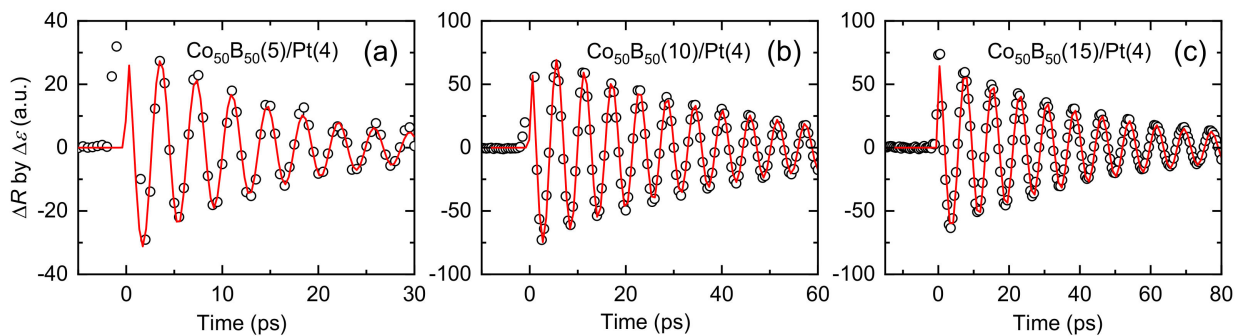


Figure 4. Acoustic oscillation. The extracted acoustic oscillation of the (a) sap/Co₅₀B₅₀ (5 nm)/Pt (4 nm), (b) sap/Co₅₀B₅₀ (10 nm)/Pt (4 nm), and (c) sap/Co₅₀B₅₀ (15 nm)/Pt (4 nm) samples. The black circles are data, and the red lines are fittings with a damped cosine function of $A \cos(2\pi ft) \exp(-t/\tau)$. The fitted f and τ : (a) $f = 270$ GHz, $\tau = 15$ ps; (b) $f = 174$ GHz, $\tau = 40$ ps; (c) $f = 129$ GHz, $\tau = 45$ ps.

Because the sapphire and Co₅₀B₅₀ had a similar Z value of $\approx 4 \times 10^7$ kg m⁻² s⁻¹, direct contact between them was not able to produce a strong acoustic oscillation. In the following, we show that a high reflection of acoustic waves was achieved due to the presence of a soft intermediate layer between Co₅₀B₅₀ and sapphire (we did not expect any soft layer at the CoB/Pt interface, because Pt was deposited immediately, in a few seconds, after the CoB deposition inside a vacuum chamber).

We extracted the thickness of the soft intermediate layer by analyzing acoustic oscillations. The frequency dependence on the transducer thickness is well understood by the speed of sound of the metal transducer (Figure 5a). Using the relationship $f = \frac{v_s}{2d_{\text{tot}}}$, where d_{tot} is the thickness of Co₅₀B₅₀+Pt and v_s is the effective speed of sound of Co₅₀B₅₀+Pt, we determined v_s to be 4900 m s⁻¹. Then, by combining f and τ , we obtained a damping parameter of $\alpha = 1/2\pi f\tau$ (Figure 5b). α describes the amplitude attenuation during one period of oscillation; it ranges from zero for no attenuation to $1/2\pi$ for full attenuation after one period. The attenuation of acoustic waves in a medium is caused by the wave transmission at interfaces and bulk attenuation inside the medium. Considering the energy conservation during the wave propagation at interfaces, the wave transmission is related to the wave reflection. Then, α can be expressed as

$$2\pi\alpha = \{1 - |r_{\text{int1}}|\} + \{1 - |r_{\text{int2}}|\} + \{1 - \exp(-2\beta_{\text{bulk}}d_{\text{tot}})\}, \quad (3)$$

where r_{int1} is the reflection coefficient at the bottom interface between the substrate and transducer, r_{int2} is the reflection coefficient at the top interface between the transducer and air, and β_{bulk} is the bulk attenuation factor in the transducer layer (we note that r can be negative when $Z_1 < Z_2$ in Equation (2), so that the reflected wave can change its sign. Since α describes the attenuation of the absolute magnitude of the acoustic wave, α should be related to $|r|$ but not r). r_{int2} was found to be close to one, considering the large

mismatch in the Z values of the transducer and air. The β_{bulk} value of metals depends on the frequency [36,37], and there are no experimental reports regarding ferromagnetic metals at a high frequency of 200 GHz. When β_{bulk} is negligible and α is dominated by r_{int1} , an α of 0.034 ± 0.011 leads to an $|r_{\text{int1}}|$ of 0.79 ± 0.07 at the $\text{Co}_{50}\text{B}_{50}/\text{sap}$ interface. When β_{bulk} is as high as $\approx 10^7 \text{ m}^{-1}$ [38], the bulk attenuation can explain most of α , and $|r_{\text{int1}}|$ will be close to one. Such a large $|r_{\text{int1}}|$ of >0.79 cannot be explained by the Z of the transducer and substrate alone; thus, a soft layer should exist at the interface. Then, r_{int1} is expressed with the acoustic properties of the soft layer [1]:

$$r_{\text{int1}} = \sqrt{\frac{Z_3^2(Z_1 - Z_2)^2 + (Z_1^2 - Z_3^2)(Z_2^2 - Z_3^2) \sin^2 \phi}{Z_3^2(Z_1 + Z_2)^2 + (Z_1^2 - Z_3^2)(Z_2^2 - Z_3^2) \sin^2 \phi}} \quad (4)$$

where $\phi = 2\pi f d_3 / v_3$; here, d_3 is the thickness of the soft layer and v_3 is the speed of sound of the soft layer. Assuming the same Z of $4 \times 10^7 \text{ kg m}^{-2} \text{ s}^{-1}$ for CoB and sapphire, and a typical Z_3 of $1.7 \pm 0.5 \times 10^6 \text{ kg m}^{-2} \text{ s}^{-1}$ and v_3 of $1.5 \pm 0.2 \text{ km s}^{-1}$ for soft materials [34,35], an $|r_{\text{int1}}|$ of $>0.79 \pm 0.07$ leads to a d_3 of $>2 \pm 1 \text{ \AA}$ at an f of 200 GHz.

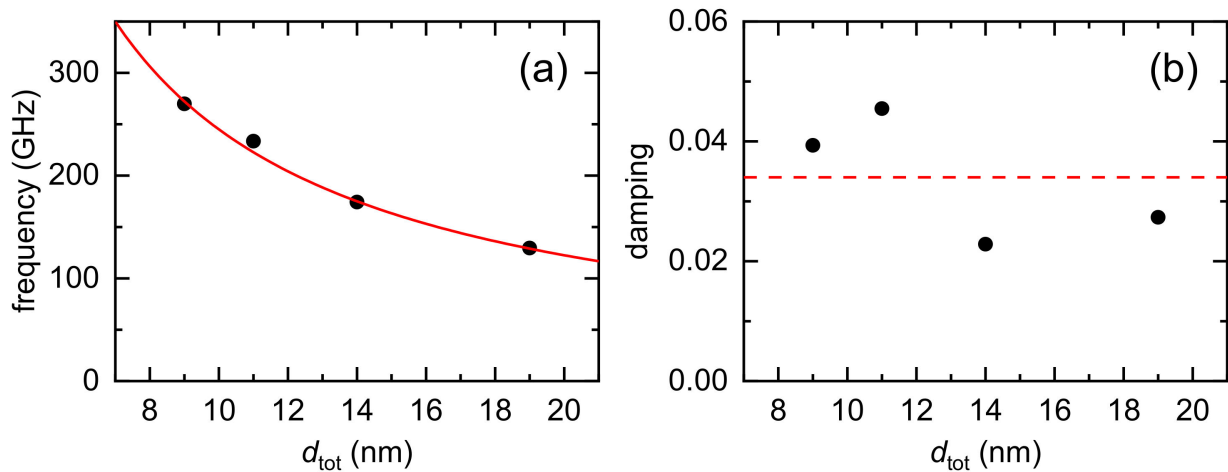


Figure 5. Frequency and damping of acoustic oscillation. (a) The frequency of the acoustic oscillation of the $\text{sap}/\text{Co}_{50}\text{B}_{50}$ (5, 7, 10, and 15 nm)/Pt (4 nm) samples. The d_{tot} represents the total thickness of $\text{Co}_{50}\text{B}_{50}$ and Pt. The red line is the fitting with $f = \frac{v_s}{2d_{\text{tot}}}$, where v_s is 4900 m s^{-1} . (b) The damping (α) of acoustic oscillations of the $\text{sap}/\text{Co}_{50}\text{B}_{50}$ (5, 7, 10, and 15 nm)/Pt (4 nm) samples. The red dotted line indicates an α of 0.034.

3.2. Heat Transport at Interface

Next, we investigated the heat transport at the interface. A thin, soft layer at the interface has a critical role in heat flow from the metal transducer to sapphire substrate. We measured the $\Delta\theta$ of the sap/Co (10 nm)/Pt (2 nm) and $\text{sap}/\text{Co}_{50}\text{B}_{50}$ (10 nm)/Pt (4 nm) samples up to 2000 ps. Then, we obtained the ratio $|\Delta\theta_{\text{in}}/\Delta\theta_{\text{out}}|$, where $\Delta\theta_{\text{in}}$ is the signal that is in-phase with the pump modulation and $\Delta\theta_{\text{out}}$ is the signal that is 90° out-of-phase with the pump modulation. This ratio makes the MOKE data more robust to errors caused by the defocusing of the pump beam and misalignment between the pump and probe beams [31–33]. The motion of the delay stage caused a slight spatial defocusing and misalignment in the pump spot on the sample, especially at long timescales of nanoseconds. The aforementioned ratio suppressed the errors associated with these issues because both $\Delta\theta_{\text{in}}$ and $\Delta\theta_{\text{out}}$ had the same dependencies on defocusing and overlap.

$\Delta\theta$ is caused by ΔM , and there are two contributions:

$$\Delta\theta \propto \Delta|M| + |M|\Delta \sin \phi, \quad (5)$$

where $|M|$ is the magnitude of magnetization and ϕ is the angle of magnetization (Figure 6a). When the magnetic field is not large enough to fully align the magnetization, a pump pulse can trigger an oscillation of ϕ . In the case of the Co transducer, the measured $|\Delta\theta_{in}/\Delta\theta_{out}|$ exhibited a large oscillation and a slow decrease (Figure 6b). With the $\text{Co}_{50}\text{B}_{50}$ transducer, a magnetic field of 0.5 T was sufficient to fully align the magnetization; there was no magnetization oscillation. The required magnetic field for the full alignment of magnetization was approximately $\mu_0 M_S$, where μ_0 is the vacuum permeability and M_S is the saturation magnetization. With an M_S of $1.4 \times 10^6 \text{ A m}^{-1}$ of Co, $\mu_0 M_S$ was 1.8 T. M_S decreased significantly with B alloying, and the $\mu_0 M_S$ of $\text{Co}_{50}\text{B}_{50}$ was smaller than 0.5 T [39]. For the thermal analysis of the Co sample, we focused on the $\Delta|M|$ signal, which was proportional to ΔT of Co, when the oscillation signal decayed completely after 500 ps.

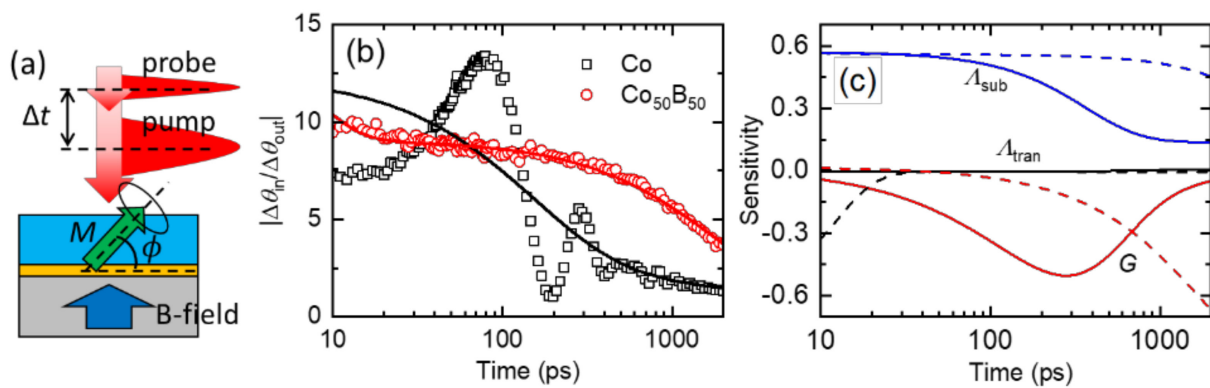


Figure 6. Analysis of heat transport. (a) Schematics for the detection of $\Delta\theta$, which is caused by changes of magnetization (M). A magnetic field (B -field) was applied to align M to the normal for the sample plane. The blue/orange/gray layers represent the transducer/interface/substrate, respectively. (b) The ratio of $|\Delta\theta_{in}/\Delta\theta_{out}|$ represents the temperature response of the magnetic transducer. The black squares and red circles are experimental data of the sap/Co (10 nm)/Pt (2 nm) and sap/ $\text{Co}_{50}\text{B}_{50}$ (10 nm)/Pt (4 nm) samples, respectively. The black and red lines are simulation results from thermal modeling with an interfacial thermal conductance of 300 and 35 $\text{MW m}^{-2} \text{K}^{-1}$, respectively. (c) The sensitivity plot for the thermal modeling to a thermodynamic parameter (γ). The black, red, and blue colors are calculation results when γ is the thermal conductivity of the transducer (Λ_{tran}), thermal conductance at the interface (G), and thermal conductivity of the substrate (Λ_{sub}), respectively. The solid and dashed lines are calculation results with the Co and CoB transducer, respectively.

We analyzed the slow decrease in $|\Delta\theta_{in}/\Delta\theta_{out}|$ using the time-domain solution of the temperature response of the top surface in the substrate/transducer structure [31]. We treated the $\text{Co}_{50}\text{B}_{50}$ and Pt layers as a single layer considering the high thermal conductance at the metallic interfaces [40]. To estimate the sensitivity of thermal modeling to a thermodynamic parameter (γ), we defined the sensitivity parameter as the logarithmic derivative of $|\Delta\theta_{in}/\Delta\theta_{out}|$ to changes in γ of the thermal model (Figure 6c):

$$S_{\gamma} = \frac{\partial[\ln(|\Delta\theta_{in}/\Delta\theta_{out}|)]}{\partial[\ln(\gamma)]}, \quad (6)$$

where γ could be the thermal conductivity (Λ) of each layer or thermal conductance (G) at the interface. The Λ of the metal transducer did not affect thermal modeling, after a few tens of ps, because of its thin thickness. The G at the interface and Λ of the substrate dominated the temperature dynamics. Because the Λ of the sapphire substrate, $30 \text{ W m}^{-1} \text{K}^{-1}$, was the same for the Co and $\text{Co}_{50}\text{B}_{50}$ samples, only G was responsible for the difference in the thermal response. When G is as high as $300 \text{ MW m}^{-2} \text{K}^{-1}$, a typical value for a strongly coupled interface between a metallic transducer and insulating substrate [23], ΔT of the transducer should decrease quickly at approximately 100 ps. By contrast, when G is as low as $35 \text{ MW m}^{-2} \text{K}^{-1}$, which is close to that of the metal/graphene/substrate interface [24,26], a significant decrease in ΔT of the transducer occurs at a much longer

timescale of 1000 ps. Such a low G value at the $\text{Co}_{50}\text{B}_{50}$ /substrate interface supports the presence of a thin, soft layer. The thermodynamic parameters for thermal modeling are summarized in Table 1.

Table 1. Thermodynamic properties for thermal analysis in Figure 6. The film structure is a sapphire substrate/metal (Co or CoB) transducer, which is presented with the thickness (d), heat capacity (C), and thermal conductivity (Λ) of each layer, and the thermal conductance (G) at the interface.

Layer	d (nm)	C ($10^6 \text{ J m}^{-3} \text{ K}^{-1}$)	Λ ($\text{W m}^{-1} \text{ K}^{-1}$)	G ($\text{MW m}^{-2} \text{ K}^{-1}$)
Co transducer	12 ¹	3.8 ⁴	100 ⁶	300 ± 50 ⁸
CoB transducer	14 ²	4.1 ⁵	20 ⁶	35 ± 5 ⁸
Substrate	500,000 ³	3.1 ⁴	30 ⁷	

¹ For the Co(10 nm)/Pt(2 nm) structure. ² For the $\text{Co}_{50}\text{B}_{50}$ (10 nm)/Pt(4 nm) structure. ³ When it is thicker than the heat penetration depth, the thickness of the substrate does not affect the thermal analysis. ⁴ [41]. ⁵ [42]. ⁶ [43]. The Λ of the transducer did not affect the thermal analysis, after a few tens of ps, because of its thin thickness. ⁷ [44]. ⁸ Fitting results.

4. Discussion

Previously, strong acoustic oscillations and low thermal conductances were achieved by inserting a two-dimensional van der Waals material, such as graphene, between the metal transducer and insulating substrate [24,26]. Graphene can withstand fabrication damage during the deposition process owing to its high mechanical stability. However, preserving a thin, soft layer with weak mechanical stability at the interface is challenging. We expect that the amorphous $\text{Co}_{50}\text{B}_{50}$ transducer can reduce the fabrication damage on the soft interface owing to its low surface binding energy (E_{sb}). Although the E_{sb} of the $\text{Co}_{50}\text{B}_{50}$ alloy has not been reported, we expect that amorphization by B alloying would have a significant effect on E_{sb} . When E_{sb} was reduced, the kinetic energy during the deposition of the metal transducer decreased (see Equation (1)).

5. Conclusions

In this study, we demonstrate that a $\text{Co}_{50}\text{B}_{50}$ transducer on top of a sapphire substrate significantly amplifies the oscillation of acoustic waves. We interpreted the strong acoustic oscillation as the existence of a thin, soft layer between the $\text{Co}_{50}\text{B}_{50}$ transducer and sapphire substrate. By analyzing the frequency and damping of acoustic oscillations, we determined the thickness of the soft layer to be $>2 \pm 1 \text{ \AA}$. In addition, owing to its magnetization, we were able to obtain the temperature information of the $\text{Co}_{50}\text{B}_{50}$ transducer. By analyzing the slow decrease in the temperature, we determined the thermal conductance at the $\text{Co}_{50}\text{B}_{50}$ /substrate interface to be $35 \pm 5 \text{ MW m}^{-2} \text{ K}^{-1}$. Such a low thermal conductance supports the presence of the thin, soft layer at the interface. Because a strong acoustic oscillation and a weak thermal conductance were not observed with the Co transducer, we inferred that the $\text{Co}_{50}\text{B}_{50}$ transducer had a critical role in reducing fabrication damage. Amorphous metals with B alloying could be used with various soft materials to investigate acoustic propagation and thermal transport.

Author Contributions: Conceptualization: G.-M.C.; Sample preparation: L.J.; TDTR investigation: L.J. and G.-M.C.; writing—original draft preparation: G.-M.C. All authors have read and agreed to the published version of the manuscript.

Funding: G.-M.C. is supported by the National Research Foundation of Korea (2019R1C1C1009199, 2018M3D1A1058793).

Institutional Review Board Statement: Not applicable.

Informed Consent Statement: Not applicable.

Data Availability Statement: Derived data supporting the findings of this study are available from the corresponding author on request.

Conflicts of Interest: The authors declare no conflict of interest.

References

1. Grahn, H.T.; Maris, H.J.; Tauc, J. Picosecond ultrasonics. *IEEE J. Quantum Electron.* **1989**, *25*, 2562–2569. [[CrossRef](#)]
2. Lin, H.N.; Stoner, R.; Maris, H.; Tauc, J. Phonon attenuation and velocity measurements in transparent materials by picosecond acoustic interferometry. *J. Appl. Phys.* **1991**, *69*, 3816–3822. [[CrossRef](#)]
3. Wright, O. Thickness and sound velocity measurement in thin transparent films with laser picosecond acoustics. *J. Appl. Phys.* **1992**, *71*, 1617–1629. [[CrossRef](#)]
4. Lee, Y.C.; Bretz, K.C.; Wise, F.W.; Sachse, W. Picosecond acoustic measurements of longitudinal wave velocity of submicron polymer films. *Appl. Phys. Lett.* **1996**, *69*, 1692–1694. [[CrossRef](#)]
5. Nye, R.A.; Kelliher, A.P.; Gaskins, J.T.; Hopkins, P.E.; Parsons, G.N. Understanding Molecular Layer Deposition Growth Mechanisms in Polyurea via Picosecond Acoustics Analysis. *Chem. Mater.* **2020**, *32*, 1553–1563. [[CrossRef](#)]
6. Bonello, B.; Perrin, B.; Romatet, E.; Jeannet, J. Application of the picosecond ultrasonic technique to the study of elastic and time-resolved thermal properties of materials. *Ultrasonics* **1997**, *35*, 223–231. [[CrossRef](#)]
7. Lee, T.; Ohmori, K.; Shin, C.-S.; Cahill, D.G.; Petrov, I.; Greene, J. Elastic constants of single-crystal TiN_x (001)(0.67 ≤ x ≤ 1.0) determined as a function of x by picosecond ultrasonic measurements. *Phys. Rev. B* **2005**, *71*, 144106. [[CrossRef](#)]
8. Mante, P.; Robillard, J.; Devos, A. Complete thin film mechanical characterization using picosecond ultrasonics and nanostructured transducers: Experimental demonstration on SiO₂. *Appl. Phys. Lett.* **2008**, *93*, 071909. [[CrossRef](#)]
9. Viel, A.; Peronne, E.; Sénépart, O.; Becerra, L.; Legay, C.; Semprez, F.; Trichet, L.; Coradin, T.; Hamraoui, A.; Belliard, L. Picosecond ultrasounds as elasticity probes in neuron-like cells models. *Appl. Phys. Lett.* **2019**, *115*, 213701. [[CrossRef](#)]
10. Thompson, E.; Manzella, E.; Murray, E.; Pelletier, M.; Stuligross, J.; Daly, B.; Lee, S.; Redwing, R. Picosecond laser ultrasonic measurements of interlayer elastic properties of 2H-MoSe₂ and 2H-WSe₂. *Mater. Today Chem.* **2020**, *18*, 100369. [[CrossRef](#)]
11. Morath, C.; Maris, H. Phonon attenuation in amorphous solids studied by picosecond ultrasonics. *Phys. Rev. B* **1996**, *54*, 203. [[CrossRef](#)]
12. Hao, H.-Y.; Maris, H.J. Study of phonon dispersion in silicon and germanium at long wavelengths using picosecond ultrasonics. *Phys. Rev. Lett.* **2000**, *84*, 5556. [[CrossRef](#)]
13. Pu, N.-W.; Bokor, J. Study of surface and bulk acoustic phonon excitations in superlattices using picosecond ultrasonics. *Phys. Rev. Lett.* **2003**, *91*, 076101. [[CrossRef](#)]
14. Devos, A.; Foret, M.; Ayrinhac, S.; Emery, P.; Rufflé, B. Hypersound damping in vitreous silica measured by picosecond acoustics. *Phys. Rev. B* **2008**, *77*, 100201. [[CrossRef](#)]
15. Daly, B.; Kang, K.; Wang, Y.; Cahill, D.G. Picosecond ultrasonic measurements of attenuation of longitudinal acoustic phonons in silicon. *Phys. Rev. B* **2009**, *80*, 174112. [[CrossRef](#)]
16. Tas, G.; Loomis, J.; Maris, H.; Bailes III, A.; Seiberling, L. Picosecond ultrasonics study of the modification of interfacial bonding by ion implantation. *Appl. Phys. Lett.* **1998**, *72*, 2235–2237. [[CrossRef](#)]
17. Rossignol, C.; Perrin, B.; Bonello, B.; Djemia, P.; Moch, P.; Hurdequint, H. Elastic properties of ultrathin permalloy/alumina multilayer films using picosecond ultrasonics and Brillouin light scattering. *Phys. Rev. B* **2004**, *70*, 094102. [[CrossRef](#)]
18. Ezzahri, Y.; Grauby, S.; Dilhaire, S.; Rampoux, J.-M.; Claeys, W. Cross-plan Si/Si Ge superlattice acoustic and thermal properties measurement by picosecond ultrasonics. *J. Appl. Phys.* **2007**, *101*, 013705. [[CrossRef](#)]
19. Hohensee, G.T.; Hsieh, W.-P.; Losego, M.D.; Cahill, D.G. Interpreting picosecond acoustics in the case of low interface stiffness. *Rev. Sci. Instrum.* **2012**, *83*, 114902. [[CrossRef](#)]
20. Swartz, E.; Pohl, R. Thermal resistance at interfaces. *Appl. Phys. Lett.* **1987**, *51*, 2200–2202. [[CrossRef](#)]
21. Stoner, R.; Maris, H. Kapitza conductance and heat flow between solids at temperatures from 50 to 300 K. *Phys. Rev. B* **1993**, *48*, 16373. [[CrossRef](#)]
22. Prasher, R.S.; Phelan, P.E. A scattering-mediated acoustic mismatch model for the prediction of thermal boundary resistance. *J. Heat Transfer* **2001**, *123*, 105–112. [[CrossRef](#)]
23. Costescu, R.M.; Wall, M.A.; Cahill, D.G. Thermal conductance of epitaxial interfaces. *Phys. Rev. B* **2003**, *67*, 054302. [[CrossRef](#)]
24. Hsieh, W.-P.; Lyons, A.S.; Pop, E.; Keblinski, P.; Cahill, D.G. Pressure tuning of the thermal conductance of weak interfaces. *Phys. Rev. B* **2011**, *84*, 184107. [[CrossRef](#)]
25. Hu, M.; Keblinski, P.; Schelling, P.K. Kapitza conductance of silicon–amorphous polyethylene interfaces by molecular dynamics simulations. *Phys. Rev. B* **2009**, *79*, 104305. [[CrossRef](#)]
26. Estrada, D.; Li, Z.; Choi, G.-M.; Dunham, S.N.; Serov, A.; Lee, J.; Meng, Y.; Lian, F.; Wang, N.C.; Perez, A. Thermal transport in layer-by-layer assembled polycrystalline graphene films. *NPJ 2D Mater. Appl.* **2019**, *3*, 1–7. [[CrossRef](#)]
27. Hasegawa, R. Present status of amorphous soft magnetic alloys. *J. Magn. Magn. Mater.* **2000**, *215*, 240–245. [[CrossRef](#)]
28. Johnson, W. Bulk amorphous metal—An emerging engineering material. *JOM* **2002**, *54*, 40–43. [[CrossRef](#)]
29. Choi, G.-M.; Min, B.-C.; Shin, K.-H. FePdB layer for perpendicular magnetic tunnel junctions. *Appl. Phys. Lett.* **2010**, *97*, 202503. [[CrossRef](#)]
30. Thompson, M.W., II. The energy spectrum of ejected atoms during the high energy sputtering of gold. *Philos. Mag.* **1968**, *18*, 377–414. [[CrossRef](#)]

31. Cahill, D.G. Analysis of heat flow in layered structures for time-domain thermoreflectance. *Rev. Sci. Instrum.* **2004**, *75*, 5119–5122. [[CrossRef](#)]
32. Kang, K.; Choi, G.-M. Thermal coupling parameters between electron, phonon, and magnon of Nickel. *J. Magn. Magn. Mater.* **2020**, *514*, 167156. [[CrossRef](#)]
33. Pham Ngoc, L.L.; Kang, K.; Choi, G.-M. The measurement of anisotropic thermal transport using time-resolved magneto-optical Kerr effect. *AIP Adv.* **2021**, *11*, 025024. [[CrossRef](#)]
34. Kinsler, L.E.; Frey, A.R.; Coppens, A.B.; Sanders, J.V. *Fundamentals of Acoustics*, 4th ed.; Wiley: Hoboken, United States, 1999.
35. Wiley. *Properties and Behavior of Polymers*, 1st ed.; Wiley: Hoboken, NJ, USA, 2011.
36. Rzyz, M.; Grabec, T.; Österreicher, J.A.; Hettich, M.; Veres, I.A. Measurement of coherent surface acoustic wave attenuation in polycrystalline aluminum. *AIP Adv.* **2018**, *8*, 125019. [[CrossRef](#)]
37. Povey, M.; Meredith, D.; Dobbs, E. Electromagnetic generation and attenuation of ultrasound in ferromagnetic metals. I. *J. Phys. F Metal Phys.* **1980**, *10*, 2041. [[CrossRef](#)]
38. Shen, X.; Lu, Z.; Timalina, Y.P.; Lu, T.-M.; Washington, M.; Yamaguchi, M. Coherent phonon transport measurement and controlled acoustic excitations using tunable acoustic phonon source in GHz-sub THz Range with variable bandwidth. *Sci. Rep.* **2018**, *8*, 1–10. [[CrossRef](#)]
39. Mizutani, U.; Hasegawa, M.; Fukamichi, K.; Hattori, Y.; Yamada, Y.; Tanaka, H.; Takayama, S. Magnetic, electronic, and electron-transport properties of amorphous $(\text{Co}_{0.85}\text{B}_{0.15})_{100-x}\text{X}_x$ ($X = \text{B}, \text{Al}, \text{Si}, \text{and V}$) alloys. *Phys. Rev. B* **1993**, *47*, 2678. [[CrossRef](#)]
40. Gundrum, B.C.; Cahill, D.G.; Averbach, R.S. Thermal conductance of metal-metal interfaces. *Phys. Rev. B* **2005**, *72*, 245426. [[CrossRef](#)]
41. Thermophysical Properties Research Center, Purdue University. *Thermophysical Properties of High Temperature Solid Materials*; Touloukian, Y.S., Ed.; Macmillan: New York, NY, USA, 1967.
42. Matsuura, M.; Mizutani, U. Low-temperature specific heat study of amorphous $\text{Co}_{1-x}\text{B}_x$ alloys. *J. Phys. F Metal Phys.* **1983**, *13*, 1539. [[CrossRef](#)]
43. Terada, Y.; Ohkubo, K.; Mohri, T.; Suzuki, T. Thermal conductivity of cobalt-base alloys. *Metall. Mater. Trans.* **2003**, *34*, 2026. [[CrossRef](#)]
44. Parchovianský, M.; Galusek, D.; Švančárek, P.; Sedláček, J.; Šajgalík, P. Thermal behavior, electrical conductivity and microstructure of hot pressed $\text{Al}_2\text{O}_3/\text{SiC}$ nanocomposites. *Ceram. Int.* **2014**, *40*, 14421–14429. [[CrossRef](#)]